J. Fluid Mech. (2022), *vol*. 937, A27, doi:10.1017/jfm.2022.122

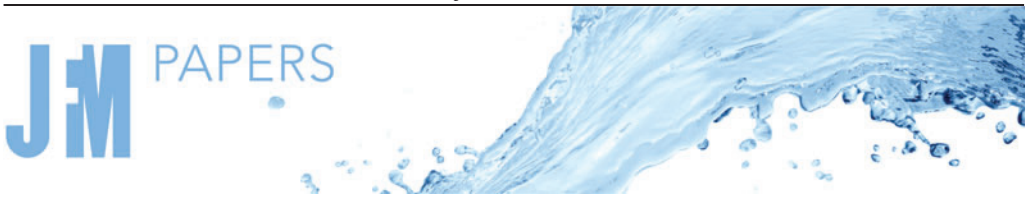

Inertio–elastic instability of a vortex column

Anubhab Roy[1],‡, **Piyush Garg**[1], **Jumpal Shashikiran Reddy**[1] and **Ganesh Subramanian**[1],†

[1]Engineering Mechanics Unit, Jawaharlal Nehru Centre for Advanced Scientific Research, Jakkur, Bangalore 560 064, India

(Received 3 January 2021; revised 30 January 2022; accepted 3 February 2022)

We analyse the instability of a vortex column in a dilute polymer solution at large Re and De with $El = De/Re$, the elasticity number, being finite. Here, $Re = \Omega_0 a^2/\nu$ and $De = \Omega_0 \tau$ are, respectively, the Reynolds and Deborah numbers based on the core angular velocity (Ω_0), the radius of the column (a), the total (solvent plus polymer) kinematic viscosity ($\nu = (\mu_s + \mu_p)/\rho$ with μ_s and μ_p being the solvent and polymer contributions to the viscosity) and the polymeric relaxation time (τ). The stability of small-amplitude perturbations in this distinguished limit is governed by the elastic Rayleigh equation whose spectrum is parameterized by $E = El(1-\beta)$, β being the ratio of the solvent to the solution viscosity. The neglect of the relaxation terms, in the said limit, implies that the polymer solution supports undamped elastic shear waves propagating relative to the base-state flow. Unlike the neutrally stable inviscid case, an instability of the vortex column arises for finite E due to a pair of elastic shear waves being driven into a resonant interaction under the differential convection by the irrotational shearing flow outside the core. An asymptotic analysis for the Rankine profile shows the absence of an elastic threshold for this instability. The growth rate is $O(\Omega_0)$ for order unity E, although it becomes transcendentally small for $E \ll 1$, being $O(\Omega_0 E^2 \mathrm{e}^{-1/E^{1/2}})$. An accompanying numerical investigation shows that the instability persists for smooth monotonically decreasing vorticity profiles, provided the radial extent of the transition region (from the rotational core to the irrotational exterior) is less than a certain E-dependent threshold.

Key words: waves in rotating fluids, vortex instability

1. Introduction

The distinguishing trait of viscoelastic fluids is an underlying microstructure that often relaxes on macroscopic time scales. For dilute polymer solutions this microstructure

† Email address for correspondence: sganesh@jncasr.ac.in
‡ Present address: Department of Applied Mechanics, Indian Institute of Technology Madras, Chennai 600 036, India.

consists of non-interacting macromolecules, the elasticity being endowed by the prolonged relaxation of these molecules on times scales which may range from milliseconds to seconds, and even longer, depending primarily on the polymer molecular weight and solvent viscosity. This elasticity has several striking consequences including rod climbing, die swell and the tubeless siphon effect which are well documented in textbooks (Bird, Armstrong & Hassager 1987).

The role of elasticity in either suppressing or triggering instabilities in various flows has also been of immense interest due to implications for the polymer and food processing industries. Approximately three decades back, the study of instabilities in polymer solutions received an impetus with the discovery of purely elastic instabilities in flows with curved streamlines, a scenario that includes the canonical viscometric flow geometries (Larson, Shaqfeh & Muller 1990; Larson 1992; Shaqfeh 1996). Such instabilities are driven by base-state hoop stresses, and the instability sets in above a threshold Deborah number (De), a dimensionless parameter denoting the ratio of the elastic to the flow time scales, even in the absence of inertia. For large curvature ratios, a statistically stationary disorderly flow results for De values above the threshold, termed elastic turbulence (Groisman & Steinberg 2000).

Elasticity also plays an important role in flows of polymer solutions where inertia is significant; a canonical and important example being the widely studied phenomenon of turbulent drag reduction (Lumley 1969; Virk 1975; White & Mungal 2008). Simulations of polymers in turbulent channel flow show suppression of the coherent structures characteristic of the buffer layer, such as counter-rotating vortices and streaks aligned with the streamwise direction, in turn leading to a reduced wall shear stress (Sureshkumar, Beris & Handler 1997; Dubief *et al.* 2004; White & Mungal 2008). Turbulent drag reduction corresponds mostly to the high Re and moderate De regimes. More recently, a novel spatiotemporally chaotic state, dubbed elasto-inertial turbulence, has been shown to arise directly from the laminar state for moderate Re and high De, and may be closely linked to the asymptotic regime of maximum drag reduction (Samanta *et al.* 2013; Choueiri, Lopez & Hof 2018; Garg *et al.* 2018; Chandra, Shankar & Das 2018; Shekar *et al.* 2019; Chaudhary *et al.* 2021). These observations call for a deeper mechanistic understanding of the inertial flows of polymeric solutions. The general question of hydrodynamic stability in the (Re, De) plane is thus an important one, and novel behaviour is expected at large Re and De (Graham 2014; Chaudhary *et al.* 2019). Towards this goal, in this paper, we study the linear stability of a vortex column in an elastic liquid (a dilute polymer solution) at large De and Re with the ratio De/Re, known as the elasticity number (El), being finite. We demonstrate that the vortex column is susceptible to a novel inertio–elastic instability in this limit.

The early numerical investigations of curvilinear flows in the large Re, De regime concern the effects of elasticity on flow stability in the Taylor–Couette (Thomas & Walters 1964, 1966; Beard, Davies & Walters 1966) and Dean geometries (Thomas & Walters 1965) for the inertially dominant case. Apart from analysing the destabilizing effect of elasticity on the centrifugal mode, these early studies led to the identification, for finite El, of the so-called inertio–elastic mode in Taylor–Couette flow (Avgousti & Beris 1993) that, unlike the centrifugal mode, had an oscillatory character at the onset. More recently, it has been shown that the inertio–elastic mode exists for all Taylor–Couette configurations with a monotonically decreasing angular velocity profile (Ogilvie & Potter 2008). There have been additional investigations of the stability of free shear flows in the inertio–elastic regime. Yarin (1997) studied the effect of polymer additives on the dynamics of a vortex filament in an ambient shear flow, and showed that vortex stretching

associated with the bending mode gets arrested by high longitudinal elastic stresses generated due to stretching of the deformed filament. Azaiez & Homsy (1994*a*) analysed the instability of a shear layer, characterized by a hyperbolic tangent velocity profile, in a dilute polymer solution. The fluid rheology was modelled using both quasilinear (Oldroyd-B, corotational Jeffreys) and nonlinear (Giesekus) constitutive relations. The authors were the first to consider the aforementioned distinguished limit, $De, Re \to \infty$ with El finite for the Oldroyd-B case, and derived the elastic Rayleigh equation that governs the stability of small-amplitude perturbations to a general parallel shearing flow in this limit. A numerical solution of this equation showed that, for finite El, elasticity stabilized the original inertial (Kelvin–Helmholtz) instability of the shear layer by truncating the unstable range of wavenumbers. As argued by Hinch (appendix of Azaiez & Homsy (1994*a*)), the stabilizing action of elasticity for long wavelength perturbations is akin to the action of surface tension in damping out transverse modulations of a stretched membrane, the tension being on account of the stretched polymers in the region of high shear (the 'membrane'). Later, motivated by the stability of vortical structures that result from the roll up of an elastic shear layer, Azaiez & Homsy (1994*b*) and Haj-Hariri & Homsy (1997) studied the role of elasticity on the stability of an unbounded linear flow with elliptical streamlines. Earlier investigations of high-Re flows of Newtonian fluids with elliptical streamlines (Kerswell 2002) show that the instability of such flows is related to the so-called elliptic instability where a vortex column, subject to an ambient straining flow, is destabilized due to a resonant interaction between pairs of Kelvin modes (Moore & Saffman 1975). These resonances correspond to points of intersection of the Kelvin dispersion curves, and can only occur in three dimensions (a finite axial wavenumber). In the elastic case, however, Haj-Hariri & Homsy (1997) found the instability to exist even in two dimensions.

The study most closely related to the current one is that of Rallison & Hinch (1995) who examined the stability of submerged planar and axisymmetric elastic jets. In addition to the expected elasticity-induced modification of the inertial instabilities known for these flow configurations, the authors identified an instability that owes its origin to an interplay of elasticity and inertia. Elastic stresses allow for the propagation of transverse shear waves along the otherwise unperturbed streamlines, and the differential convection by the base-state shear leads to the resonant interaction of a shear-wave pair, in turn leading to exponential growth. The inertio–elastic instability of the vortex column studied here has a similar underlying physical mechanism. An important advantage of the vortex column configuration is that it is inertially stable; as shown recently, the Rankine vortex only supports neutrally stable discrete and continuous spectrum (CS) modes, a combination of which may at best lead to algebraic growth for short times (Roy & Subramanian 2014*b*; Roy 2013); analogous results hold for smooth monotonically decaying vorticity profiles. Hence, unlike all earlier efforts (Azaiez & Homsy 1994*a*; Rallison & Hinch 1995; Haj-Hariri & Homsy 1997) where the flow configurations are also susceptible to purely inertial instabilities, the novel inertio–elastic instability in the vortex case exists in isolation. Further, for both the jet and vortex cases, the inertio–elastic instability appears to require a sharp spatial transition from a region that strongly stretches the polymer molecules to a relatively quiescent region where the polymer molecules are close to their equilibrium coil configurations.

In this paper, we examine the aforementioned inertio–elastic instability, analytically for a Rankine vortex, and numerically for other smooth monotonically decreasing vorticity profiles, for two-dimensional disturbances with zero axial wavenumber. The examination of smooth vorticity profiles allows one to verify the requirement of a sharp transition

region which, for a vortex column, would be from a central region of solid-body rotation to an irrotational point-vortex exterior. The paper is organized as follows. In § 2, starting from the equations of motion and the Oldroyd-B constitutive relation, we derive the governing linearized equations for small-amplitude perturbations at finite De and Re. Next, we obtain the elastic Rayleigh equation in plane polar coordinates that governs the stability of a base-state vortical flow to infinitesimal perturbations in the limit $Re, De \to \infty$ with El finite. The dimensionless parameter governing stability in this distinguished limit is $E = El(1-\beta)$. In § 3, we examine the exponential instability that arises for an elastic vortex column via a shear wave resonance; this involves numerically investigating the smooth vorticity profiles above for finite E (§ 3.1), and an analytical-cum-numerical investigation of the Rankine profile for small E (§ 3.2). The discrete unstable mode for the Rankine profile is closely related to the elastic CS for small E. In this limit, it propagates with an angular speed slower than that of the core by an amount of $O(E^{1/2})$ and with a transcendentally small growth rate of $O(E^2 \mathrm{e}^{-E^{-1/2}})$, in units of the core angular velocity, both determined using a matched asymptotics expansion approach; the predictions are in good agreement with numerical results, obtained using a shooting method, for sufficiently high resolution. The transcendental scaling above leads to a precipitous drop in the growth rate for small E in the numerics, similar to that observed earlier, but not analysed, for the submerged elastic jet (Rallison & Hinch 1995). Numerical results for more general vorticity profiles, where the discontinuity in the base-state vorticity of the Rankine vortex is smoothened into a transition layer of width d, show that the instability persists for non-Rankine profiles, and that the growth rate is of the order of the core angular velocity for finite E. Finally, in § 4, we summarize the main results with a discussion of future lines of research that emerge from this effort. The vortex stability problem analysed here also has astrophysical ramifications owing to the direct analogy between the governing equations of polymer dynamics for large De and those of magnetohydrodynamics (MHD) at large magnetic Reynolds numbers (Re_m); and these are also discussed in § 4.

2. Problem formulation: the elastic Rayleigh equation

The equations of motion and continuity for a polymer solution of density ρ are given by

$$\rho \frac{\mathrm{D}\boldsymbol{v}}{\mathrm{D}t} = -\boldsymbol{\nabla} p^* + \boldsymbol{\nabla} \cdot \boldsymbol{\sigma}_d, \tag{2.1}$$

$$\boldsymbol{\nabla} \cdot \boldsymbol{v} = 0, \tag{2.2}$$

where $\boldsymbol{\sigma}_d$, the deviatoric stress, is assumed to satisfy the Oldroyd-B constitutive equation and the rescaled pressure, p^*, accounts for the additional (osmotic) pressure induced by polymer molecules. The Oldroyd-B relation is one of the simplest constitutive relations that offers a semiquantitative description of nearly constant viscosity dilute polymer solutions known as Boger fluids (James 2009), and corresponds to a microscopic description where the polymer molecules are modelled as non-interacting Hookean dumbbells (Bird *et al.* 1987; Larson 1988). For simple shear flow, the Oldroyd-B relation predicts a constant shear viscosity and first normal stress difference coefficient, and a zero second normal stress difference. It is convenient to write $\boldsymbol{\sigma}_d$ in (2.1) as the sum of solvent and polymer contributions, $\boldsymbol{\sigma}_d = 2\mu_s \boldsymbol{E} + G\boldsymbol{A}$. Here, $\boldsymbol{E} = \boldsymbol{\nabla v} + (\boldsymbol{\nabla v})^\dagger$ is the rate of strain tensor with μ_s being the solvent viscosity. The polymer stress contribution is proportional to the shear modulus G with the conformation tensor $\boldsymbol{A} \propto \langle \boldsymbol{RR} \rangle$, $\boldsymbol{R}$ being the dumbbell end-to-end vector. Since the dumbbells respond affinely to an imposed velocity field in the

absence of relaxation, $\boldsymbol{A}$ is governed by

$$\overset{\triangledown}{\boldsymbol{A}} = -\frac{1}{\tau}(\boldsymbol{A} - \boldsymbol{I}), \tag{2.3}$$

where τ is the relaxation time and '$\triangledown$' denotes the upper-convected derivative defined by

$$\overset{\triangledown}{\boldsymbol{X}} \equiv \frac{\mathrm{D}\boldsymbol{X}}{\mathrm{D}t} - (\boldsymbol{\nabla v})^{\dagger} \cdot \boldsymbol{X} - \boldsymbol{X} \cdot (\boldsymbol{\nabla v}), \tag{2.4}$$

with $\mathrm{D}/\mathrm{D}t$ being the material derivative. One may now rewrite the governing set of equations as

$$\rho \frac{\mathrm{D}\boldsymbol{v}}{\mathrm{D}t} = -\boldsymbol{\nabla} p^{*} + \mu_s \nabla^2 \boldsymbol{v} + G \boldsymbol{\nabla} \cdot \boldsymbol{A}, \tag{2.5}$$

$$\boldsymbol{\nabla} \cdot \boldsymbol{v} = 0, \tag{2.6}$$

$$\frac{\mathrm{D}\boldsymbol{A}}{\mathrm{D}t} - (\boldsymbol{\nabla v})^{\dagger} \cdot \boldsymbol{A} - \boldsymbol{A} \cdot (\boldsymbol{\nabla v}) = -\frac{1}{\tau}(\boldsymbol{A} - \boldsymbol{I}). \tag{2.7}$$

To examine the linearized evolution of two-dimensional disturbances in the swirling flow of an Oldroyd-B fluid, we write $\boldsymbol{v} = \bar{\boldsymbol{u}} + \boldsymbol{u}, \boldsymbol{A} = \bar{\boldsymbol{A}} + \boldsymbol{a}$ for the velocity and polymer stress fields with the overbar quantities denoting the unperturbed base state. In the regime of interest in this paper ($Re, De \to \infty$), any general axisymmetric swirling flow $\bar{\boldsymbol{u}} = (0, \Omega(r)r, 0)$, with $\Omega(r)$ the angular velocity, is an exact solution of the equations of motion. The associated base-state stresses are given by

$$\bar{\boldsymbol{A}} = \begin{bmatrix} 1 & r\Omega'\tau \\ r\Omega'\tau & 1 + 2(r\Omega'\tau)^2 \end{bmatrix} \tag{2.8}$$

in a cylindrical coordinate system where $'$ denotes a radial derivative. The base-state hoop stress component ($\bar{\boldsymbol{A}}_{\theta\theta}$), on account of the quadratic scaling with the shear rate, becomes dominant for large shear rates ($r\Omega'\tau \gg 1$) except when $\Omega' = 0$ which corresponds to the trivial case of solid-body rotation. In what follows, we analyse the linear stability of the Rankine vortex profile for which $\Omega(r) = \Omega_0$ for $r < a$ (the rigidly rotating core) and $\Omega(r) = \Omega_0(a/r)^2$ for $r \geq a$ (the irrotational exterior). We also examine the linear stability of more general vorticity profiles numerically.

The governing equation for the perturbation velocity field is

$$\frac{\partial \boldsymbol{u}}{\partial t} + \Omega \frac{\partial \boldsymbol{u}}{\partial \theta} + \boldsymbol{u} \cdot \boldsymbol{\nabla} \bar{\boldsymbol{u}} = -\frac{1}{\rho}\boldsymbol{\nabla} p + \nu_s \nabla^2 \boldsymbol{u} + \frac{G}{\rho}\boldsymbol{\nabla} \cdot \boldsymbol{a}. \tag{2.9}$$

For the two-dimensional perturbations under consideration, $\boldsymbol{u} \equiv (u_r, u_\theta)$, and the formulation is more convenient in terms of the axial vorticity, w_z, which satisfies the following equation:

$$\begin{aligned} \left(\frac{\partial}{\partial t} + \Omega \frac{\partial}{\partial \theta}\right) w_z + u_r DZ &= \nu_s \nabla^2 w_z + \frac{G}{\rho}\{\boldsymbol{\nabla} \wedge (\boldsymbol{\nabla} \cdot \boldsymbol{a})\}_z \\ &= \nu_s \nabla^2 w_z + \frac{G}{\rho}\left[\frac{1}{r^2}\frac{\partial^2}{\partial r \partial \theta}(rN_1) + \frac{1}{r}\frac{\partial}{\partial r}\left(\frac{1}{r}\frac{\partial}{\partial r}(r^2 a_{r\theta})\right) - \frac{1}{r^2}\frac{\partial^2}{\partial \theta^2} a_{r\theta}\right]. \end{aligned} \tag{2.10}$$

Here, $DZ = r\Omega'' + 3\Omega'$ is the base-state vorticity gradient and $N_1 = a_{\theta\theta} - a_{rr}$ is the perturbation to the first normal stress difference. For the Rankine vortex, the

base-state vorticity (Z) and vorticity gradient (DZ) are $Z(r) = 2\Omega_0\mathcal{H}(a-r)$ and $DZ(r) = -2\Omega_0\delta(r-a)$, with $\mathcal{H}(z)$ and $\delta(z)$ being the Heaviside and Dirac delta functions, respectively.

The perturbation elastic stress components that appear in (2.10) obey the following equations:

$$\left(\frac{\partial}{\partial t} + \Omega\frac{\partial}{\partial\theta} + \frac{1}{\tau}\right)a_{rr} - 2\left\{\bar{A}_{rr}\frac{\partial u_r}{\partial r} + \frac{\bar{A}_{r\theta}}{r}\frac{\partial u_r}{\partial\theta}\right\} = 0, \tag{2.11}$$

$$\left(\frac{\partial}{\partial t} + \Omega\frac{\partial}{\partial\theta} + \frac{1}{\tau}\right)a_{r\theta} + \left\{\bar{A}'_{r\theta}u_r - \bar{A}_{r\theta}\left(\frac{\partial u_r}{\partial r} + \frac{u_r}{r}\right) - \frac{\bar{A}_{\theta\theta}}{r}\frac{\partial u_r}{\partial\theta}\right\} + \left\{\bar{A}_{rr}\left(\frac{u_\theta}{r} - \frac{\partial u_\theta}{\partial r}\right) - \frac{\bar{A}_{r\theta}}{r}\frac{\partial u_\theta}{\partial\theta}\right\} - r\Omega' a_{rr} = 0, \tag{2.12}$$

$$\left(\frac{\partial}{\partial t} + \Omega\frac{\partial}{\partial\theta} + \frac{1}{\tau}\right)a_{\theta\theta} - 2\left\{\bar{A}_{r\theta}\left(\frac{\partial u_\theta}{\partial r} - \frac{u_\theta}{r}\right) + \frac{\bar{A}_{\theta\theta}}{r}\frac{\partial u_\theta}{\partial\theta}\right\} + \left(\bar{A}'_{\theta\theta} - \frac{2\bar{A}_{\theta\theta}}{r}\right)u_r - 2r\Omega' a_{r\theta} = 0. \tag{2.13}$$

We use the vortex core radius a as the length scale and the turnover time based on the core angular frequency Ω_0^{-1} as a time scale. Next, assume a normal mode form, $h(r,\theta) = \hat{h}(r)\mathrm{e}^{\mathrm{i}(m\theta-\omega t)}$, for the various perturbation fields, where m is the azimuthal wavenumber and ω is the complex-valued frequency with $\mathrm{Im}(\omega) > 0$ corresponding to an exponentially growing perturbation. Thus, from (2.10) and (2.11)–(2.13), we obtain the following non-dimensional equations governing the r-dependent perturbation amplitudes:

$$\Sigma r\mathcal{L}(r\hat{u}_r) + mrDZ\hat{u}_r = \frac{\mathrm{i}}{Re}r\mathcal{L}^2(r\hat{u}_r) - \frac{\mathrm{i}m}{Ma_e^2}\left[-mD^*\hat{N}_1 + \mathrm{i}DD^*(r\hat{a}_{r\theta}) + \frac{\mathrm{i}m^2}{r}\hat{a}_{r\theta}\right], \tag{2.14}$$

$$\Sigma_2\hat{a}_{rr} = 2\mathrm{i}\left\{\bar{A}_{rr}D + \frac{\mathrm{i}m\bar{A}_{r\theta}}{r}\right\}\hat{u}_r, \tag{2.15}$$

$$\Sigma_2\hat{a}_{r\theta} = -\frac{r\bar{A}_{rr}}{m}DD^*\hat{u}_r - \left\{\frac{m}{r}\bar{A}_{\theta\theta} + \mathrm{i}\bar{A}'_{r\theta}\right\}\hat{u}_r + \mathrm{i}\hat{a}_{rr}r\Omega', \tag{2.16}$$

$$\Sigma_2\hat{a}_{\theta\theta} = -\frac{2r\bar{A}_{r\theta}}{m}DD^*\hat{u}_r - \mathrm{i}\left\{\bar{A}'_{\theta\theta} + 2\bar{A}_{\theta\theta}D\right\}\hat{u}_r + 2\mathrm{i}\hat{a}_{r\theta}r\Omega', \tag{2.17}$$

where

$$D = \frac{\mathrm{d}}{\mathrm{d}r}, \quad D^* = \frac{\mathrm{d}}{\mathrm{d}r} + \frac{1}{r}, \quad \Sigma(r) = \omega - m\Omega(r) \quad \text{and} \quad \Sigma_2(r) = \omega - m\Omega(r) + \frac{\mathrm{i}}{De}, \tag{2.18a–d}$$

and the non-dimensional base-state polymeric stresses are given by (2.8) with τ replaced by De. Here, we have used the relation $\hat{w}_z = (\mathrm{i}/m)\mathcal{L}(r\hat{u}_r)$ between the axial vorticity and radial velocity perturbations for zero axial wavenumber with $\mathcal{L} = DD^* - (m^2-1)/r^2$ (Roy & Subramanian 2014*b*). The non-dimensional parameters in (2.14)–(2.17) are the Deborah number, $De = \Omega_0\tau$ which is the ratio of the relaxation to the flow time scale, the Reynolds number, $Re = \Omega_0 a^2/\nu$ based on the total viscosity $\mu = \mu_s + \mu_p = \mu_s + G\tau$

and the elastic Mach number, $Ma_e = \Omega_0 a/c_{elas}$ where $c_{elas} = \sqrt{G/\rho}$ is the shear wave speed in a quiescent elastic medium. (Note that De is used here instead of the Weissenberg number which is sometimes used in both the drag reduction and elastic instability literature; the distinction between the two parameters is not relevant in the present context.) Similar to its counterpart in compressible flows, Ma_e may be interpreted as the ratio of a characteristic flow velocity scale to the speed of propagation of infinitesimal amplitude shear stress (or vorticity) fluctuations in a quiescent incompressible elastic medium. The elastic Mach number may be written in terms of Re and De as $Ma_e^2 = (1/(1-\beta))DeRe$, $\beta = \mu_s/\mu$ being the ratio of the solvent to the total viscosity, and for a fixed β, the evolution of the perturbations, as governed by (2.14)–(2.17), depends therefore on Re and De. Here $\beta = 0$ corresponds to a upper-convected Maxwell (UCM) fluid while $\beta = 1$ corresponds to a Newtonian fluid; in the latter case, $Ma_e \to \infty$, and (2.14) with only the first term on the right-hand side is the Orr–Sommerfeld equation in cylindrical coordinates.

The above system of equations may be combined into a single fourth-order differential equation governing $\hat{u}_r$, the cylindrical analogue of the viscoelastic Orr–Sommerfeld equation that has been examined earlier in the context of plane parallel flows (Renardy & Renardy 1986). Apart from discrete modes, for any finite De and Re, the system (2.14)–(2.17), similar to the case of parallel shear flows, possesses a pair of continuous spectra. The latter are given by $r \epsilon r_c$ with r_c defined by

$$\Sigma_2(r_c) = 0, \tag{2.19}$$

$$\Sigma(r_c) + \frac{\mathrm{i}}{\beta De} = 0, \tag{2.20}$$

where $\Sigma_2(r)$ and $\Sigma(r)$ are as defined above (Renardy & Renardy 1986; Wilson, Renardy & Renardy 1999; Kupferman 2005). For $Re = \infty$, there also arises the well known inviscid CS, given by $\Sigma(r_c) = 0$, and spanning the base-state range of angular velocities (Roy & Subramanian 2014*a*,*b*). However, with Re finite and for a bounded domain, the continuous spectra arise solely due to the additional viscoelastic terms (Chaudhary *et al.* 2019).

The relation (2.19) defines the Gorodtsov–Leonov (GL) CS (Gorodtsov & Leonov 1967), named after the authors who originally discovered it for inertialess plane Couette flow of a UCM fluid. Although usually studied in the aforementioned specific context owing to its analytical tractability (Graham 1998), the GL spectrum continues to exist for finite Re, and for both parallel shear flows and the azimuthal shearing flows considered here. Its origin is the assumed local nature of the polymeric stress field in almost all constitutive equations in polymer rheology (Bird *et al.* 1987). The evolution of the polymeric stress field in the absence of centre-of-mass diffusion is, in fact, similar to that of the vorticity field in the inviscid limit, and both cases, in principle, allow for arbitrarily large gradients across streamlines (Roy & Subramanian 2014*b*,*a*). Based on this analogy, one expects CS modes with singularities in the polymeric stress fields. The singular GL-eigenfunctions, in addition to being convected with the flow velocity at $r = r_c$, decay at a rate De^{-1} due to relaxation, asymptoting to neutral stability for $De \to \infty$. Further, similar to the plane parallel case, the GL spectrum in cylindrical coordinates is characterized by the Frobenius exponents 0, 1, 3 and 4, the streamline curvature being negligible on the length scales defining the validity of the local Frobenius analysis. An additional CS arises due to a finite solvent viscosity (Wilson *et al.* 1999), being pushed off to infinity in the UCM limit ($\beta \to 0$). Again, similar to the parallel flow case, this viscous singular CS has Frobenius exponents – 0, 1, 2 and $3 - 2/\beta$. The final fractional Frobenius exponent indicates the existence of an algebraic branch point and an associated branch cut (Kupferman 2005).

The CS eigenfunctions in this case require, therefore, a principal-finite-part interpretation (Engevik 1971; Gakhov 1990; Roy & Subramanian 2014*b*).

We now proceed to the regime of interest, $Re \to \infty$ with $El = De/Re = \nu\tau/a^2$ fixed, in which case (2.14)–(2.17), with the neglect of the $O(De^{-1})$ terms denoting microstructural relaxation, yields the following equation governing u_r:

$$\begin{aligned}\Sigma^3[\Sigma(r^2D^2\hat{u}_r + 3rD\hat{u}_r - (m^2-1)\hat{u}_r) + mrDZ\hat{u}_r] \\ = 2m^2E\Omega'[\Sigma^2\{r^2\Omega'D^2\hat{u}_r + r(r\Omega'' + DZ)D\hat{u}_r \\ - (m^2-1)\Omega'\hat{u}_r\} + mr\Omega'\Sigma\{2r\Omega'D\hat{u}_r + 3(DZ - 2\Omega')\hat{u}_r\} + 2m^2r^2\Omega'^3\hat{u}_r],\end{aligned} \tag{2.21}$$

which is the elastic Rayleigh equation with $E = El(1-\beta)$; the terms proportional to E in (2.21) denote the contributions due to elasticity. Thus, the original fourth-order ordinary differential equation resulting from (2.14)–(2.17) reduces to a second-order ordinary differential equation in the limit $De \to \infty$, El, β fixed, implying that the neglect of relaxation is a singular limit. From what is known for the eigenfunctions of the Rayleigh and Orr–Sommerfeld equations (see section 5 in Roy & Subramanian (2014*a*)), one expects a non-trivial relationship between the spectrum of the elastic Rayleigh equation and that associated with the full set of equations for large but finite De. The viscosity ratio β no longer plays a fundamental role as for finite De where a non-zero β leads to an additional CS; in the above limit, one may interpret a change in β in terms of a rescaled E.

For typical inertio–elastic flows, El is the governing parameter only for small but finite De when relaxation effects are dominant and the fluid rheology is describable in terms of a retarded motion expansion (see, for instance, Dabade, Navaneeth & Subramanian (2015)). For large De, relaxation is unimportant with the dynamics in the polymeric fluid at finite Re being governed by elastic shear waves damped due to the solvent viscosity alone. In this limit, Ma_e becomes the governing parameter (Joseph 2007). It is thus a little surprising that in the limit of large De considered here, El rather than Ma_e turns out to be relevant for (2.21), suggesting the continued importance of relaxation ($El \propto \tau$). However, El in (2.21) is more appropriately interpreted in terms of a viscoelastic Mach number where the sonic speed corresponds to shear waves propagating in a prestressed elastic medium. The base-state stress level is $\bar{A}_{\theta\theta} \sim O(De^2)$ as given earlier, and the shear wave speed relevant to the perturbation dynamics is given by $\sqrt{G\bar{A}_{\theta\theta}/\rho} \sim De\sqrt{G/\rho}$. The relevant Mach number is $O(De).O(\sqrt{G/\rho}/\Omega_0 a) \sim (De/Re)^{1/2} \sim El^{1/2}$. Thus, the rather paradoxical dependence on El, and thence on the relaxation time, occurs via the shear wave speed being dependent on the base-state hoop stress. Note that the assumption of the base-state stresses being dependent on the relaxation time, but the perturbations not being sensitive to it, is analogous to the usual assumption for Newtonian fluids where the base state is assumed to be determined by slow viscous diffusion at large Re, but the latter is nevertheless assumed to play a negligible role in the dynamics of perturbations.

One may rewrite (2.21), in a compact form, in terms of the radial displacement ($\xi \equiv \mathrm{i}\hat{u}_r/\Sigma$) as

$$D[r^3PD\xi] = r(m^2-1)P\xi, \tag{2.22}$$

where $P = \Sigma^2 - 2m^2E\Omega'^2$. This form was first identified by (Rallison & Hinch 1995) in the context of parallel shearing flows. From (2.22), one may easily construct the following modified version of Howard's semicircle theorem (Howard 1962) for swirling flows:

$$\left(\omega_r - \frac{m(\Omega_{max} + \Omega_{min})}{2}\right)^2 + \omega_i^2 \le m^2\left(\frac{\Omega_{max} - \Omega_{min}}{2}\right)^2 - 2m^2E\,{\Omega'_{min}}^2. \tag{2.23}$$

The role of elasticity is to shrink the inviscid semicircle of instability, implying a relative stabilization. The analogue of (2.22) has been used by Rallison & Hinch (1995) in their study of elastic instabilities in jets. Stability to exponentially growing perturbations results when the semicircle radius decreases to zero, and this happens at a finite E provided Ω'_{min} is non-zero. A novel mechanism of instability, associated with the elastic Rayleigh equation, and that may arise even for non-inflectional profiles, is that resulting from the resonant interaction of elastic shear waves. The shear waves propagate more rapidly (relative to the flow) with increasing E, and the onset of stability above coincides with the inability of the base-state shear, beyond a threshold E, to bring a pair of such waves into resonance. Note that the form (2.22) also implies the existence of a pair of continuous spectra corresponding to fore- and aft-propagating singular elastic shear waves. The waves propagate with an angular speed of $O(\sqrt{E})$ relative to the flow, and are obtained by setting $P = \Sigma^2 - 2m^2 E\Omega'^2 = 0$. These travelling-wave spectra are in addition to the original inviscid CS (Case 1960; Roy & Subramanian 2014*b*) modified by elasticity. Keeping in mind the significance of the elastic CS in interpreting the discrete unstable mode for small E (see figure 6 below), a more detailed discussion of the same is included in the supplementary material available at https://doi.org/10.1017/jfm.2022.122.

3. Shear wave resonance instability of a vortex column

In this section, we show that a vortex in a viscoelastic fluid is susceptible to a two-dimensional instability. Towards this end, we first numerically examine the spectra of Rankine-like smooth vorticity profiles as a function of E (§ 3.1). For small E, the unstable eigenfunction is a regularized version of a travelling wave comprising the elastic CS, the travelling wave singularities cut off due to a finite growth rate (see the discussion of the CS in the supplementary material). For the specific case of a Rankine vortex, the elastic instability is then analysed via a matched asymptotic expansions approach valid for small E (§ 3.2).

3.1. *Numerical calculation of the unstable mode*

The Rankine vortex has a compact vorticity profile with a step discontinuity at the core radius. A smooth vorticity profile, convenient for use in the numerical calculations below, is given by

$$Z(r) = \frac{Z_0}{2}\left\{1 - \tanh\left[\frac{r-a}{d}\right]\right\}. \tag{3.1}$$

Here, d is the length scale over which there is a smooth transition from the core vortical region to the exterior irrotational one, with $d \to 0$ denoting the limit of a Rankine vortex.

3.1.1. *Details of the numerical method*

Stability investigations in the limit for large Re and De suffer from numerical issues, largely due to the presence of the continuous spectra in the elastic Rayleigh equation (Miller 2005). For the problem under consideration, two additional effects make the investigation of the unstable mode a difficult one for small E. First, the unstable mode asymptotes to a singular neutral mode (a part of the CS) in the limit $E \to 0$. This is unlike the classical inviscid problem where the unstable mode approaches a regular neutral mode, the so-called S-wave, close to the threshold (Drazin & Howard 1966; Drazin & Reid 1981). The second reason is the emergence of a transcendentally small length scale for small

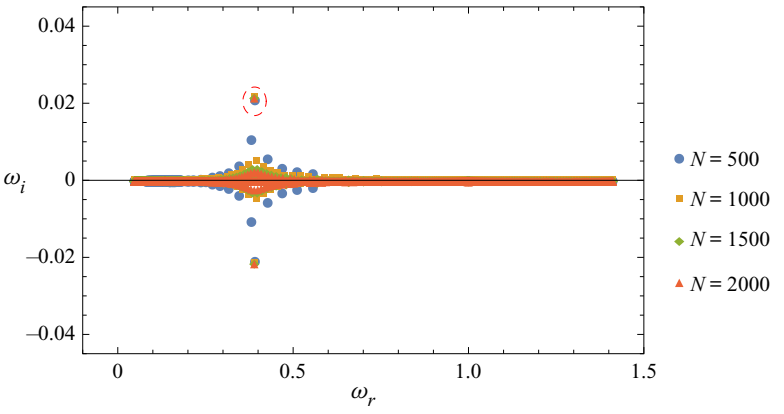

Figure 1. Collapse of the ballooned spectrum with increasing number of collocation points (N) for the vorticity profile defined in (3.1) with $d = 0.025, a = 1$ for $E = 0.1$; the domain is $r \in (0, r_\infty)$ with $r_\infty = 4a$. The converged unstable mode is encircled.

E (identified as part of the analysis in the next section). The inability of the numerics, for a fixed resolution, to resolve the aforementioned small scale, leads to an inevitable breakdown below $E \approx 0.02$ regardless of the approach used.

For the smooth monotonically decreasing vorticity profile in (3.1), two separate formulations of the eigenvalue problem in (2.22) are studied. In the first formulation, the linear eigenvalue problem given by (2.14)–(2.17) (in the limit $Re, De \to \infty$) is solved using Chebyshev collocation. In the second formulation, a solution of the nonlinear eigenvalue problem (2.22) for ξ is obtained using a compound matrix method wherein the original nonlinear eigenvalue problem is written as a higher-dimensional linear one, which is then solved using standard Chebyshev collocation (Bridges & Morris 1984; Roy 2013). Both formulations yield consistent results, and here we show results from the second formulation (Roy 2013). The spectral method obtains the entire eigenspectrum, including the singular elastic continuous spectra alluded to at the end of § 2. Since the CS modes are not C^∞, the neutral continuous spectra manifest as balloons in the numerical spectrum and for a modest number of collocation points, the ballooned CS ends up engulfing the unstable mode (Roy 2013; Chaudhary *et al.* 2019). As shown in figure 1, it is only for a sufficiently large number of collocation points (N) that the CS balloon shrinks sufficiently for the converged discrete mode to be identified.

The Rankine vortex, on account of the singular base-state vorticity profile, cannot be studied using spectral methods, and a regular shooting method is applied using the inbuilt bvp4c command in MATLAB. The resolution ($\tilde{N}$) of the shooting method is controlled by the number of mesh points used for the spatial discretization for the numerical integration in MATLAB. Now $\tilde{N} = 8000$, unless explicitly mentioned otherwise, for the results obtained below using the shooting method. Here, we only solve (2.22) for $r > a$, with appropriate boundary conditions at the core (irrotational) exterior interface (see (3.6)–(3.7) in § 3.2). Owing to the difficulty arising from the extreme sensitivity of the eigenvalue found to the initial guess, we use a 'carpet bombing' technique to obtain a reasonably accurate initial guess of the eigenvalue (Miller 2005). Herein, one of the boundary conditions is allowed to be an unknown, its difference from the true boundary condition being termed the 'error'. This error is then minimized on a complex-ω grid to arrive at the initial guess (see Roy (2013) for details).

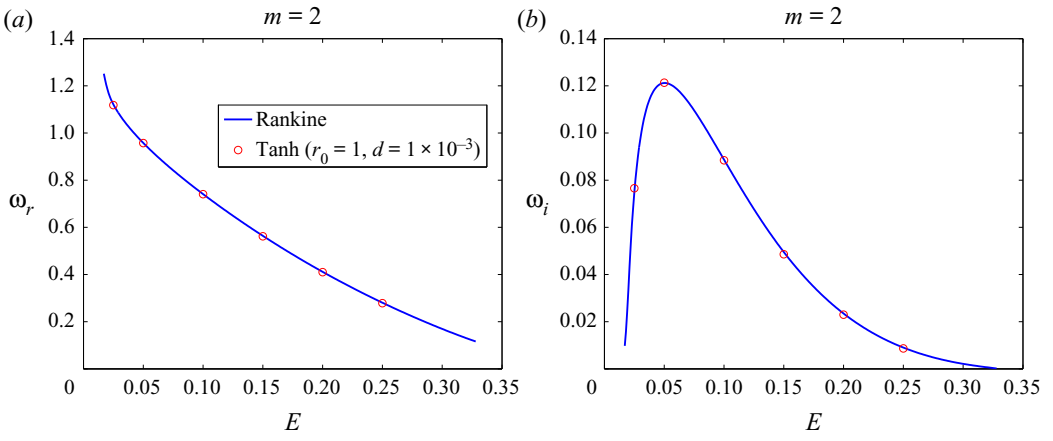

Figure 2. Wave speed (*a*) and growth rate (*b*) comparisons between a Rankine vortex (shooting method) and the smooth vortex in (3.1) with $a = 1$ and $d = 10^{-3}$ (spectral method), for $m = 2$. Note that the numerical method does not provide reliable results below $E \approx 0.02$, and the suggestion of an elastic threshold in (*b*) is misleading; the perturbation analysis in § 3.2 shows that the instability persists for any non-zero E (also see the higher resolution results, in figure 8, in this regard).

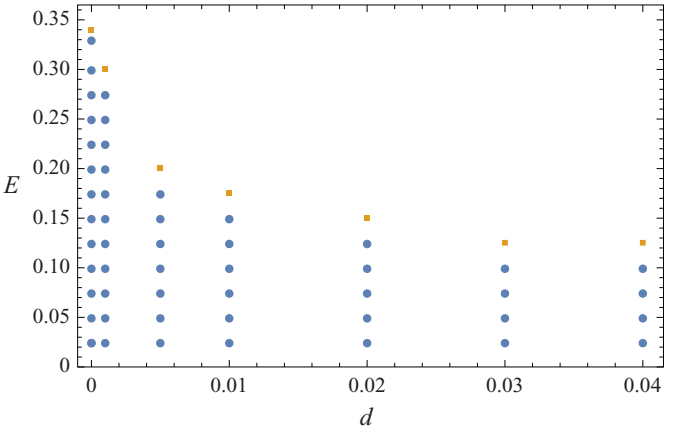

Figure 3. The region of instability for the smooth vortex (3.1) for varying E and the smoothness parameter d, with $a = 1$ and $m = 2$; the domain is $r \in (0, r_\infty)$ with $r_\infty = 4a$. The (blue) circles denote the parameters for which a converged unstable mode was obtained, and the (orange) squares denote the parameters for which such a mode could not be found for N up to 3000. For $d = 0$ (the Rankine vortex), the symbols correspond to results obtained using the shooting method.

3.1.2. *Numerical results for the inertio–elastic instability*

Figure 2(*a*,*b*) shows both results from the spectral code (red symbols), for the smooth vortex defined by (3.1) for $d = 10^{-3}$, and that obtained from the shooting method for the Rankine profile. The close comparison of the growth rate and the wave speed shows that an inertio–elastic instability exists for both a Rankine vortex and Rankine-like smooth vorticity profiles. For a smooth profile, one expects the transition width (d), the region over which the flow transitions from a rigid-body rotation to an irrotational straining one, to determine the existence of the instability. Expectedly, figure 3 shows that instability exists for a narrower range of E with increasing d.

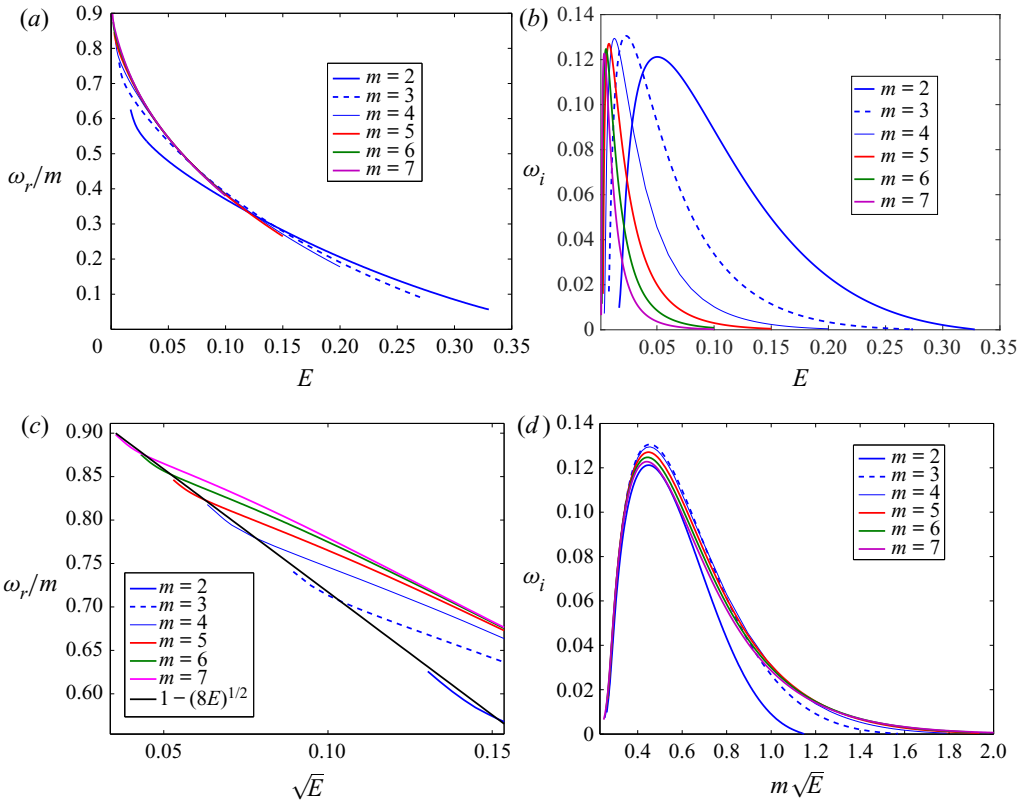

Figure 4. Dependence of the wave speed (a) and growth rate (b) on E for various values of m. In (c) the phase speed is compared with the leading-order asymptotic solution, $\omega_r = m(1 - \sqrt{8E})$ (§ 3.2), while (d) shows the collapse of the ω_i curves when plotted as a function of $m\sqrt{E}$. Note that the numerical method does not provide reliable results for ω_i below $E \approx 0.02$. However, the perturbation analysis in § 3.2 shows that the instability persists for any non-zero E.

From here on, we focus on the Rankine vortex, and thus all the results presented are computed using the shooting method. Figure 4(a,b) shows the dependence of the wave speed and growth rate of the unstable mode on E for different m. Figure 4(c) shows the convergence of the wave speeds for different m to a common asymptote, given by $1 - \sqrt{8E}$, in the limit $E \to 0$. Figure 4(d) highlights the dependence of the growth rate on the rescaled azimuthal wavenumber $m\sqrt{E}$. Note that the collapse occurs for $m\sqrt{E} \sim O(1)$ and m sufficiently large, and accordingly, the curves for the lowest m ($m = 2$ and 3) deviate from the scaled form. Figure 4(d) also shows a rather precipitous drop in growth rate for small E, leading to an eventual breakdown of the numerics (for the chosen resolution) below $E \approx 0.02$. As argued in the next section, the steep drop and the associated breakdown arise from a transcendental scaling of the eigenvalue for small E.

The eigenfunctions for both the radial displacement and velocity fields are shown in figure 5. The twin peaks in the eigenfunction profiles correspond to the fore- (larger r) and aft- (smaller r) shear wave locations; these peaks become singular in the limit $E \to 0$, as the eigenfunction asymptotes to a singular travelling wave eigenfunction in the elastic CS. Figure 6 quantifies this approach by plotting the real parts of the radial

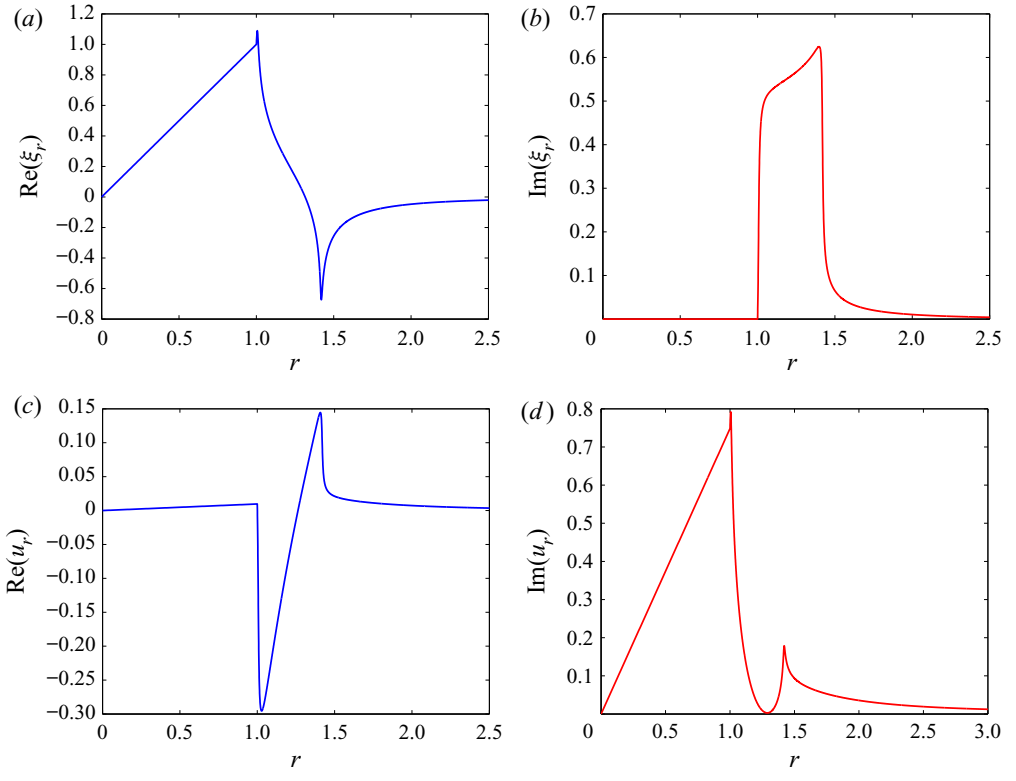

Figure 5. Real and imaginary parts of the radial displacement (*a*,*b*) and velocity eigenfunctions (*c*,*d*) for the unstable mode for $E = 0.017$, $m = 2$.

displacement eigenfunctions, for a sequence of E tending to zero, and a CS eigenfunction for sufficiently small E. This resemblance, along with the conformance of the wave speed of the unstable mode to the elastic shear wave scaling ($\omega_r \sim 1 - \sqrt{8E}$, see figure 4*c*), points to the inertio–elastic instability resulting from a resonant interaction between the elastic shear waves, which, for small E, propagate at nearly the same speed near the vortex core (Rallison & Hinch 1995; Miller 2005). The shear wave resonance argument also explains why the instability continues to exist for smooth Rankine-like profiles as is seen from figure 3.

3.2. *A matched asymptotic analysis for the inertio–elastic instability of a Rankine vortex: $E \ll 1$*

In this subsection, we analyse the elastic Rayleigh equation, (2.22), for the Rankine profile. This profile exhibits a complete separation of the rotational and straining regions. The polymer molecules in the vortex core are unaffected by solid-body rotation, and retain their equilibrium distribution of conformations. Thus, the polymer stress is homogeneous and isotropic and the solution for $r < 1$ is identical to the inviscid case, with $u_r \propto r^{m-1}$. In order to obtain a normalized radial displacement, the constant of proportionality is chosen to be $\Sigma_0 = \omega - m$; as a result, $\xi = r^{m-1}$ and $\mathrm{d}\xi/\mathrm{d}r|_{r=1-} = m - 1$.

The radial displacement in the core, derived above, may now be used as part of a boundary condition for that in the exterior, governed by (2.22) written in an expanded

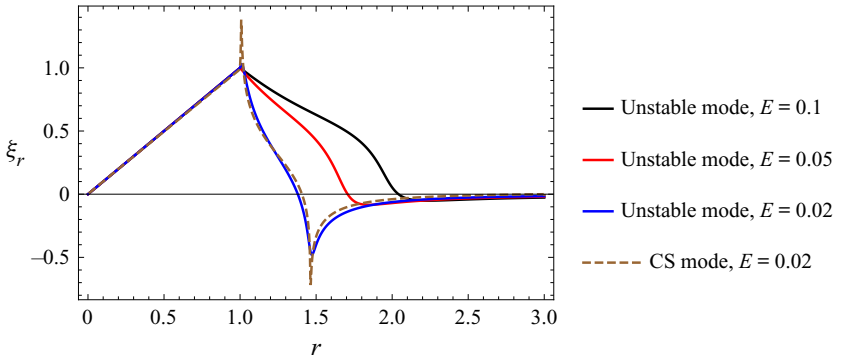

Figure 6. Real part of the radial displacement eigenfunction for the unstable mode for varying E; a neutral mode from the CS for $E = 0.02$, and with the same wave speed, is shown for comparison.

form as

$$D[r^3\{(\omega - m\Omega)^2 - 2m^2E\Omega'^2\}D\xi] = r(m^2-1)\{(\omega - m\Omega)^2 - 2m^2E\Omega'^2\}\xi. \tag{3.2}$$

Noting that the radial displacement is continuous, that is, $\xi|_{r=1+} = \xi|_{r=1-} = 1$ and integrating (2.22) across $r = 1$, one obtains

$$\left[r^3 P\frac{\mathrm{d}\xi}{dr}\right]_{r=1-}^{r=1+} = 0, \tag{3.3}$$

$$\Rightarrow \quad \{\Sigma_0^2 - 8E(m\Omega_0)^2\}\left.\frac{\mathrm{d}\xi}{\mathrm{d}r}\right|_{r=1+} - \Sigma_0^2\left.\frac{\mathrm{d}\xi}{\mathrm{d}r}\right|_{r=1-} = 0, \tag{3.4}$$

$$\Rightarrow \quad \left.\frac{\mathrm{d}\xi}{\mathrm{d}r}\right|_{r=1+} = \frac{(m-1)(\omega-m)^2}{(\omega-m)^2 - 8m^2E}, \tag{3.5}$$

where the expression for the radial displacement gradient in the core is used in the last step. The above condition is combined with the usual requirement of decay in the far field. To summarize the problem statement, the radial displacement in the irrotational exterior satisfies (3.2), and is subject to the following boundary conditions:

$$\xi|_{r=1} = 1, \tag{3.6}$$

$$\left.\frac{\mathrm{d}\xi}{\mathrm{d}r}\right|_{r=1+} = \frac{(m-1)(\omega-m)^2}{(\omega-m)^2 - 8m^2E}, \tag{3.7}$$

$$\xi \to 0, \quad \text{as } r \to \infty. \tag{3.8}$$

The collapse of the growth rate curves for various m, in figure 4(d), suggests $m\sqrt{E}$ as the parameter relevant to the asymptotics of the unstable mode for small E. This can also be seen in (3.2), where the term $(\omega - m\Omega)^2 - 2m^2E\Omega'^2$ involves the interplay of inertia and elasticity, with a balance implying $(\omega - m\Omega) \sim \pm m\sqrt{2E}\Omega'$. For a near-neutral mode, this balance occurs near the vortex core edge, $r \approx 1$, implying $(\omega - m) \sim \pm m\sqrt{8E}$ since $\Omega' = -2$ at $r = 1$. Thus, the elastic stresses for this mode are localized about the critical radius, $r_c \sim 1 + O(\sqrt{E})$. This suggests the introduction of a rescaled boundary layer coordinate

$x = (r-1)/\sqrt{E}$ with $\omega = m(1 - a_1\sqrt{E})$, where a_1 is the unknown eigenvalue. In the limit $E \to 0$ with $m\sqrt{E}$ fixed, this leads to the following simplified equation:

$$\frac{\mathrm{d}}{\mathrm{d}x}\left[\{(a_1 - 2x)^2 - 8\}\frac{\mathrm{d}\xi}{\mathrm{d}x}\right] = m^2 E\{(a_1 - 2x)^2 - 8\}\xi, \tag{3.9}$$

subject to the boundary conditions

$$\xi|_{x=0} = 1, \tag{3.10}$$

$$\left.\frac{\mathrm{d}\xi}{\mathrm{d}x}\right|_{x=0} = \sqrt{E}\frac{(m-1)(\omega - m)^2}{(\omega - m)^2 - 8m^2E} = m\sqrt{E}\frac{a_1^2}{a_1^2 - 8}, \tag{3.11}$$

$$\xi \to 0, \quad \text{as } x \to \infty, \tag{3.12}$$

which contain only the parameter $m\sqrt{E}$, as anticipated. The above equation is of the confluent Heun form, although recognition of this fact is not helpful from the perspective of obtaining closed form analytic solutions for $m\sqrt{E} \sim O(1)$ (Rallison & Hinch 1995; Renardy 2008).

Thus, to make analytical progress we consider the alternate limit $E \ll 1$ for $m \sim O(1)$. This also helps clarify the absence of a threshold E for the instability – an aspect that, as already seen, is not resolved by the numerics (as is evident in figure 4*d*). However, in this limit, apart from the obvious length scale of $O(\sqrt{E})$, a transcendentally small (in E) length scale emerges from consideration of the boundary conditions. To see this, consider the boundary layer equation (3.9) which takes the form

$$\frac{\mathrm{d}}{\mathrm{d}x}\left[\{(a_1 - 2x)^2 - 8\}\frac{\mathrm{d}\xi}{\mathrm{d}x}\right] = 0. \tag{3.13}$$

The right-hand side of (3.9) has been discarded, being asymptotically small for $m \sim O(1)$. Equation (3.13) has solutions of the form

$$\xi = c_1 + c_2 \log\left[\frac{2x - a_1 - \sqrt{8}}{2x - a_1 + \sqrt{8}}\right], \tag{3.14}$$

with the boundary conditions,

$$\xi|_{x=0} = 1, \tag{3.15}$$

$$\left.\frac{\mathrm{d}\xi}{\mathrm{d}x}\right|_{x=0} = \sqrt{E}\frac{(m-1)(\omega - m)^2}{(\omega - m)^2 - 8m^2E} = \sqrt{E}\frac{(m-1)a_1^2}{a_1^2 - 8}, \tag{3.16}$$

$$\xi \to 0, \quad \text{as } x \to \infty. \tag{3.17}$$

The far-field decay required by (3.17) implies that $c_1 = 0$ in (3.14). Applying the gradient boundary condition, (3.16), we have $c_2 = (m-1)a_1^2\sqrt{E}/(8\sqrt{2})$. Next, considering (3.15),

one obtains

$$\xi|_{x=0} = \frac{(m-1)a_1^2\sqrt{E}}{8\sqrt{2}} \log\left[\frac{a_1+\sqrt{8}}{a_1-\sqrt{8}}\right] = 1. \tag{3.18}$$

Since $a_1 \sim O(1)$ the above relation can only be satisfied if

$$a_1 = \sqrt{8} + 2\sqrt{8}\exp\left(-\frac{1}{m-1}\sqrt{\frac{2}{E}}\right)a_2, \tag{3.19}$$

where a_2 is an $O(1)$ constant. Although we have added a seemingly exponentially small quantity to the expected $O(1)$ estimate, this addition is crucial in the normal displacement boundary condition. With the transcendentally small addition, the normal displacement gradient, given by (3.16), is found to be exponentially large. This obviously contradicts the algebraic scaling assumed in (3.16), and highlights the subtle nature of the small E limit. Physically, the locations $x = a_1 + \sqrt{8}$ and $x = a_1 - \sqrt{8}$ correspond, in rescaled form, to the fore- and aft-moving shear wave singularities. Since $a_1 - \sqrt{8} \sim \exp(-(1/(m-1))(\sqrt{2/E}))$, the implication is that the aft-travelling shear wave is separated from the edge of the core only by a transcendentally small amount. Note that the above contradiction is not an artefact of the order in which we choose to satisfy the boundary conditions above. The underlying transcendental scaling also explains the precipitous drop in the growth rate (similar to that in figure 4*d*) of the elastic instability in a submerged jet observed by Rallison & Hinch (1995) – see figure 7 therein.

Thus, we see a crucial difference between the eigenfunction structure in the two limits analysed above. For $E \to 0$ with $m\sqrt{E}$ fixed, both the forward- and backward-travelling shear waves lie within a boundary layer with a thickness of $\sqrt{E}$, next to the vortex core, this being the only length scale of relevance. However, in the limit $E \ll 1$ for $m \sim O(1)$, the above arguments show that while the forward-travelling shear wave is still localized in an $O(\sqrt{E})$ boundary layer, the backward-travelling wave is only separated from the edge of the core by a transcendentally small distance of $O(\exp(-(1/(m-1))(\sqrt{2/E})))$. Thus, the perturbation analysis in this latter case needs to recognize two different length scales, one of them exponentially smaller than the other. The asymptotic framework must accordingly include an additional inner boundary layer with $r - 1 \sim O(g\sqrt{E})$ satisfying the boundary conditions at $r = 1$ (g will turn out to be transcendentally small). The outer $O(\sqrt{E})$ boundary layer is therefore no longer constrained to satisfy the boundary conditions at $r = 1$, resolving the contradiction in the naive approach above. Instead, it matches onto both the inner boundary layer and the outer regions in the appropriate limits. Figure 7 shows the different asymptotic regions for a numerically evaluated radial displacement eigenfunction. We thus have the following double expansion, for the eigenvalue, in the limit $g \ll 1, E \ll 1$:

$$\frac{\omega}{m} = 1 - \sqrt{E}[\sqrt{8} + g\{c_0 + c_1\sqrt{E} + c_2E + c_3E^{3/2} + \ldots\} + O(g^2)]. \tag{3.20}$$

Note that, in neglecting the contributions at $O(g^2)$ and higher, we anticipate the transcendental smallness of g in (3.20), owing to which terms of $O(g)$ are, in principle, smaller than any algebraic order in E; that $g \sim \exp(-(1/(m-1))(\sqrt{2/E}))$ emerges from the detailed analysis given below, and the expansion in (3.20) conforms to the exponential asymptotics formalism (Boyd 1999). Note that the $O(g)$ contribution is crucial despite its transcendental smallness, since it contributes to the leading-order growth rate.

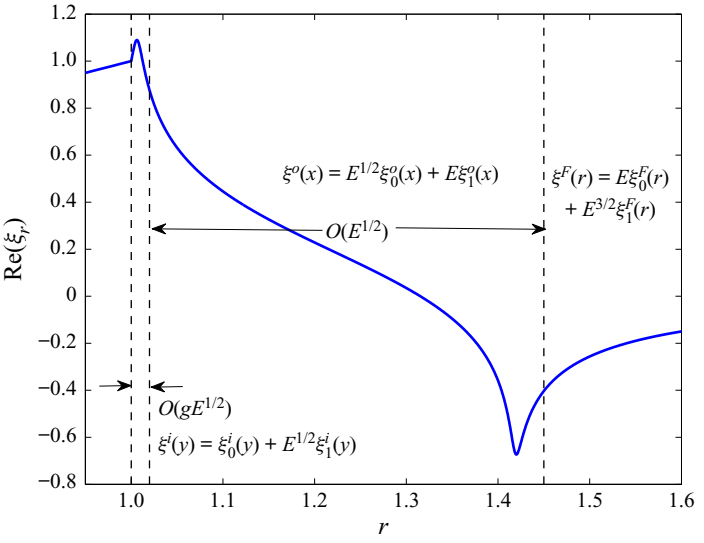

Figure 7. Numerically evaluated radial displacement eigenfunction illustrating the nested boundary layer structure that characterizes the small-E asymptotic analysis discussed in the text: $r < 1$, the vortex core; $r > 1$ with $r - 1 \sim O(g\sqrt{E})$, the inner boundary layer; $r > 1$ with $r - 1 \sim O(\sqrt{E})$, the outer boundary layer; $r > 1$ with $r - 1 \sim O(1)$, the outer region.

It is shown below that the growth rate is $O(E^2 \mathrm{e}^{-1/\sqrt{E}})$ for small E, and, therefore, also transcendentally small. Importantly, however, this establishes the absence of a threshold for the elastic instability in contrast to what is suggested by the numerical results above (figure 4*d*).

The matched asymptotic expansions approach used here may be validated by consideration of an exactly soluble subproblem – that governed solely by the left-hand side of (3.2) – termed the left-hand side problem herein. The agreement of the asymptotic approach with the small-E expansion of the exact solution serves as a useful validation both of the exponential asymptotics formalism, and the additional subtle feature of phase jumps across the shear-wave singularities; the analysis of the left-hand side problem is detailed in the supplementary material. In what follows, we present a brief synopsis of the analogous analysis, of the full equation (2.22) for small E, recognizing the different asymptotic regions mentioned above. The detailed analysis is again given in the supplementary material following the analysis of the left-hand side problem.

3.2.1. *Outer region:* $r - 1 \sim O(1)$

To begin with, we study the solution in the region where $r - 1 \sim O(1)$. Expanding P in the elastic Rayleigh equation (2.22) for small E, one obtains

$$\frac{P}{m^2} = \mathcal{S}_0 + \sqrt{E}\mathcal{S}_1 + E\mathcal{S}_2 + O(g\sqrt{E}), \tag{3.21}$$

where

$$\mathcal{S}_0 = \left(1 - \frac{1}{r^2}\right)^2, \quad \mathcal{S}_1 = -2\sqrt{8}\left(1 - \frac{1}{r^2}\right) \quad \text{and} \quad \mathcal{S}_2 = 8\left(1 - \frac{1}{r^6}\right). \tag{3.22a–c}$$

The expansion of P has terms which scale algebraically with $\sqrt{E}$ as well as terms that are transcendentally small (of $O(g)$). At leading order, we only need to consider the finite number (three) of terms in (3.21) that scale algebraically. The unknown eigenvalue constants (the c_i) in (3.20) lead to transcendentally small contributions, and, hence, do not enter the expansion for P and the outer region analysis at leading order. Denoting the displacement by $\xi^F(r)$, the above points to the following expansion:

$$\xi^F(r) = E\,\xi_0^F(r) + E^{3/2}\,\xi_1^F(r) + O(E^2) + O(g\sqrt{E}), \tag{3.23}$$

where we again neglect the transcendentally smaller contributions. While the $O(E)$ scaling of the leading-order term is evident from the matching considerations below (see § 3.2.4), it may nevertheless be anticipated based on the discussion above. The aft-shear-wave is located in an exponentially small neighbourhood of the edge of the core, and the (logarithmic) displacement due to this wave decreases by $O(\sqrt{E})$ in the outer boundary layer which is exponentially distant when measured in units of the inner boundary layer thickness of $O(g\sqrt{E})$. Further, the near cancellation between the $O(\sqrt{E})$ displacements associated with the fore- and aft-shear-waves for $r-1 \sim O(1)$ leads to an asymptotically smaller ξ^F of $O(E)$ in this outer region (see figure 7), as assumed in the expansion above. The solution in the outer region, to $O(E^{3/2})$, is as follows:

$$\xi^F(r) = E\frac{\mathcal{B}_0}{r^{m-1}(r^2-1)} + E^{3/2}\left\{\frac{2\sqrt{2}\mathcal{B}_0}{r^{m-1}(r^2-1)^2} + \frac{\mathcal{B}_1}{r^{m-1}(r^2-1)}\right\} + O(E^2). \tag{3.24}$$

As already mentioned, the details of the aforementioned solution are given in the supplementary material. In the outer region solution (ξ^F), there are no signatures of the travelling shear-wave singularities. Note that we do not consider the $O(E^2)$ and higher-order contributions to ξ^F since they are not required to determine the growth rate at leading order, an insight that is obtained from the solution of the left-hand side problem.

3.2.2. *Outer boundary layer: $r-1 \sim O(\sqrt{E})$*

Having found the solution in the outer region, we now consider the outer boundary layer using the boundary layer coordinate $x = (r-1)/\sqrt{E}$ already introduced at the beginning of this section. Denoting the boundary layer displacement as $\xi(r) = \xi^o(x)$, one obtains the rescaled elastic Rayleigh equation as

$$\frac{\mathrm{d}}{\mathrm{d}x}\left[\mathcal{Q}\frac{\mathrm{d}\xi^o}{\mathrm{d}x}\right] = \frac{E\mathcal{Q}(m^2-1)}{(1+\sqrt{E}x)^2}\xi^o, \tag{3.25}$$

where $\mathcal{Q} = (1+\sqrt{E}x)^3 P/m^2E$, and is further expanded as

$$\mathcal{Q} = \mathcal{Q}_0 + \sqrt{E}\mathcal{Q}_1 + E\mathcal{Q}_2 + E^{3/2}\mathcal{Q}_3 + O(E^2) + O(g\sqrt{E}), \tag{3.26}$$

with $\mathcal{Q}_0 = 4x(x-2\sqrt{2})$, $\mathcal{Q}_1 = -12\sqrt{2}x(x-2\sqrt{2})$, $\mathcal{Q}_2 = x^2(x^2-4\sqrt{2}x-24)$ and $\mathcal{Q}_3 = x^3(88-x^2)$. Similar to the expansion of P discussed earlier in § 3.2.1, the transcendentally small terms are again neglected in (3.26). The displacement (ξ^o) may thus be expanded as

$$\xi^o(x) = \sqrt{E}\,\xi_0^o(x) + E\,\xi_1^o(x) + E^{3/2}\,\xi_2^o(x) + E^2\,\xi_3^o(x) + O(E^{5/2}) + O(g\sqrt{E}). \tag{3.27}$$

where the leading $O(\sqrt{E})$ scaling is consistent with the aforementioned physical arguments. Substituting the above expansion into (3.25), one obtains the following

equation at $O(\sqrt{E})$ for the leading-order boundary layer displacement:

$$\frac{\mathrm{d}}{\mathrm{d}x}\left[\mathcal{Q}_0\frac{\mathrm{d}\xi_0^o}{\mathrm{d}x}\right]=0 \tag{3.28}$$

$$\Rightarrow \quad \xi_0^o(x)=\mathcal{G}_{10}+\mathcal{G}_{11}\log\left(\frac{x-2\sqrt{2}}{x}\right). \tag{3.29}$$

In the expression above, the forward and backward travelling wave singularities correspond to $x=2\sqrt{2}$ and $x=0$, respectively; the latter location is the edge of the core, since transcendentally small terms are now neglected. The details of the solutions at higher orders are given in the supplementary material.

The constant $\mathcal{G}_{10}$ in (3.29) is determined via matching, the details of which are again given in the supplementary material. We only note here that in deriving the limiting forms of the above solutions for $x\to 0$, required for matching, one has to account for the multivaluedness of the logarithm in the displacement field ($\xi_0^o(x)$) in (3.29). Recall that $x=2\sqrt{2}$ marks the location (singularity) of the neutrally stable forward-travelling shear wave. The neutral stability arises because the (imaginary) growth rate appears at a higher (and transcendentally small) order in the perturbation expansion. This leads to an ambiguity in the phase jump associated with the logarithm, that is well known in inviscid hydrodynamic stability (Drazin & Reid 1981). The resolution involves displacing the aforementioned shear-wave singularity off the real axis to $x=2\sqrt{2}-\mathrm{i}\epsilon$, with $\epsilon>0$ representative of the small but finite growth rate. As a result, one has

$$\begin{aligned}\log(x-2\sqrt{2}+\mathrm{i}\epsilon)&=\log|x-2\sqrt{2}| \quad x>2\sqrt{2},\\ &=\log|x-2\sqrt{2}|+\mathrm{i}\pi \quad x<2\sqrt{2}.\end{aligned} \tag{3.30}$$

The above relation may now be used in obtaining the limiting forms of the outer boundary layer solutions.

3.2.3. *Inner boundary layer: $r-1\sim O(g\sqrt{E})$*

Finally, we introduce an inner boundary layer in an exponentially small neighbourhood of the core, corresponding to $O(1)$ values of the boundary layer coordinate $y=(r-1)/g\sqrt{E}$ with $g, E\ll 1$. Denoting the inner boundary layer displacement as $\xi(r)=\xi^i(y)$, we have from (3.2)–(3.7) that

$$\frac{\mathrm{d}}{\mathrm{d}y}\left[\mathcal{R}\frac{\mathrm{d}\xi^i}{\mathrm{d}y}\right]=\frac{g^2E\mathcal{R}(m^2-1)}{(1+g\sqrt{E}y)^2}\xi^i, \tag{3.31}$$

with $\mathcal{R}=(1+g\sqrt{E}y)^3P/(m^2gE)$, which is further expanded as

$$\mathcal{R}=\mathcal{R}_0+\sqrt{E}\mathcal{R}_1+O(E), \tag{3.32}$$

where $\mathcal{R}_0=4\sqrt{2}(c_0-2y)$ and $\mathcal{R}_1=4\sqrt{2}(c_1+6\sqrt{2}y)$. Note that this is the first instance where the unknown eigenvalue constants (the c_i) enter the expansion. In anticipation of the transcendental smallness of g, we assume $gE^{-\alpha}\to 0$ as $E\to 0$, $\forall\,\alpha>0$, which allows the neglect of the right-hand side term in (3.2) at all orders. The boundary conditions at

the core-exterior interface, (3.6) and (3.7), take the form

$$\xi^i(y=0)=1, \tag{3.33}$$

$$\frac{\mathrm{d}\xi^i}{\mathrm{d}y}(y=0)=(m-1)\sqrt{E}\left\{\frac{\sqrt{2}}{c_0}-\frac{\sqrt{2}c_1\sqrt{E}}{c_0^2}+\ldots\right\}. \tag{3.34}$$

Guided by the above expansions the boundary layer variable, $\xi^i(y)$, is expanded as follows:

$$\xi^i(y)=\xi_0^i(y)+\sqrt{E}\,\xi_1^i(y)+E\,\xi_2^i(y)+O(E^{3/2})+O(g\sqrt{E}), \tag{3.35}$$

where we note that the radial displacement is now $O(1)$, as dictated by the boundary condition (3.33). Plugging the above expansion in (3.31) and using the boundary conditions (3.33) and (3.34), we have the following equations (and boundary conditions) and solutions at successive orders.

At $O(1)$ we obtain

$$\frac{\mathrm{d}}{\mathrm{d}y}\left[\mathcal{R}_0\frac{\mathrm{d}\xi_0^i}{\mathrm{d}y}\right]=0, \tag{3.36}$$

with $\xi_0^i(y=0)=1$ and $(\mathrm{d}\xi_0^i/\mathrm{d}y)(y=0)=0$, which gives

$$\xi_0^i(y)=1. \tag{3.37}$$

At $O(E^{1/2})$ we obtain

$$\frac{\mathrm{d}}{\mathrm{d}y}\left[\mathcal{R}_0\frac{\mathrm{d}\xi_1^i}{\mathrm{d}y}\right]=0, \tag{3.38}$$

with $\xi_1^i(y=0)=0$ and $(\mathrm{d}\xi_1^i/\mathrm{d}y)(y=0)=\sqrt{2}(m-1)/c_0$, which gives

$$\xi_1^i(y)=-\frac{(m-1)}{\sqrt{2}}\log\left(\frac{c_0-2y}{c_0}\right). \tag{3.39}$$

From the expression for $\xi_1^i(y)$ and the solutions at higher orders below, we see that the singularity associated with the backward-travelling shear wave is now resolved, and corresponds to $y=c_0/2$ ($x=gc_0/2$), where c_0 still needs to be determined.

At $O(E)$ we obtain

$$\frac{\mathrm{d}}{\mathrm{d}y}\left[\mathcal{R}_0\frac{\mathrm{d}\xi_2^i}{\mathrm{d}y}\right]=-\frac{\mathrm{d}}{\mathrm{d}y}\left[\mathcal{R}_1\frac{\mathrm{d}\xi_1^i}{\mathrm{d}y}\right], \tag{3.40}$$

with $\xi_2^i=0$ and $\mathrm{d}\xi_2^i/\mathrm{d}y=-(\sqrt{2}(m-1)c_1/c_0^2)$, which gives

$$\xi_2^i(y)=-3(m-1)\log\left(\frac{c_0-2y}{c_0}\right)-\frac{(m-1)}{2}(\sqrt{2}c_1+6c_0)\left\{\frac{1}{c_0-2y}-\frac{1}{c_0}\right\}. \tag{3.41}$$

The expansion (3.35) with the solutions given by (3.37)–(3.41), satisfies the boundary conditions at the vortex core ($y=0$), and, further, needs to be matched to the solution in the outer boundary layer, which will yield the values of the constants $c_0, c_1, \ldots$ in the eigenvalue expansion. In the matching region ($y \gg 1$), one again needs to account for the phase jump associated with the logarithm. This is done along the lines of the discussion above, in the context of the outer boundary layer, by noting that the singularity of the

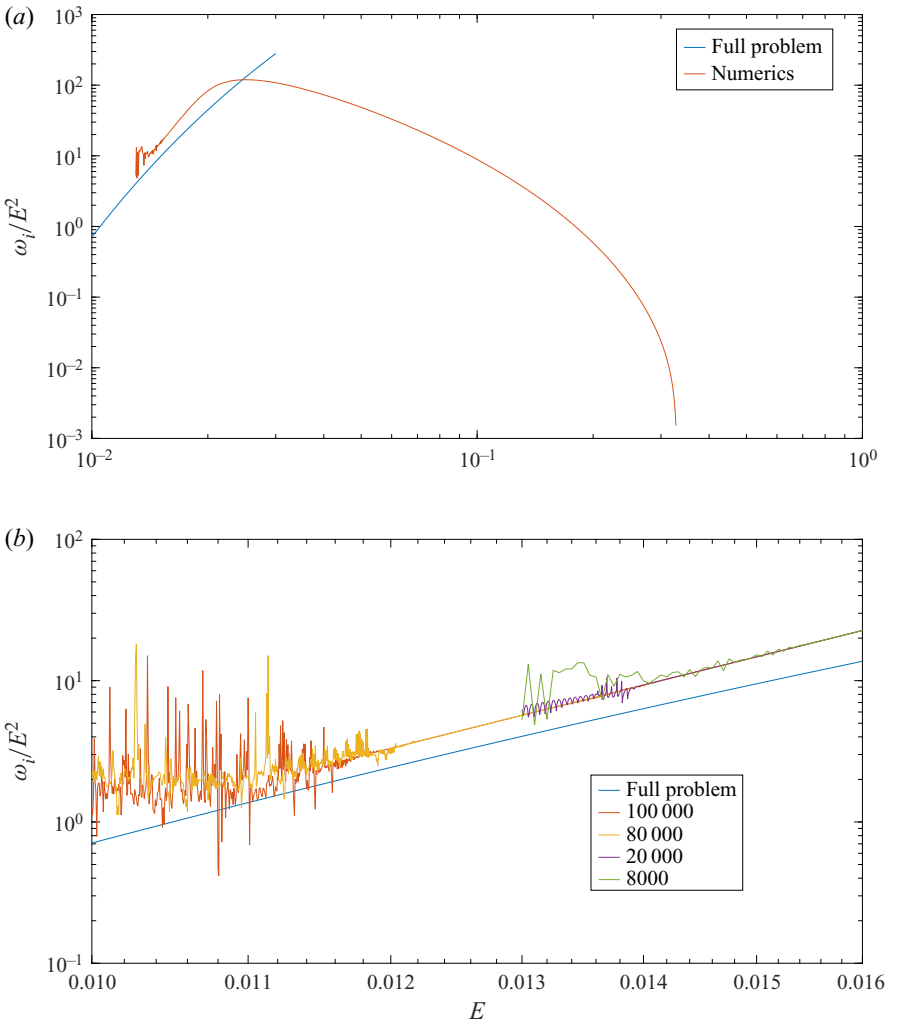

Figure 8. (*a*) Comparison of the numerical growth rate ($\tilde{N} = 8000$) and the analytical predictions for the full problem (see (3.43)) for $m = 2$. (*b*) The breakdown of the numerical results at progressively smaller E with increasing resolution ($\tilde{N}$) of the shooting method; here, $\tilde{N}$ refers to the number of mesh points used for the spatial discretization for the numerical integration in the shooting method.

unstable mode, associated with the backward-travelling shear wave, lies off the real axis at $y = c_0/2 - \mathrm{i}\epsilon'$ ($\epsilon' > 0$), and one therefore has the relations

$$\begin{aligned} \log(c_0 - 2y - 2\mathrm{i}\epsilon') &= \log|c_0 - 2y|, \qquad y < \frac{c_0}{2}, \\ &= \log|c_0 - 2y| - \mathrm{i}\pi, \quad y > \frac{c_0}{2}. \end{aligned} \tag{3.42}$$

3.2.4. *Matching*

With the inner, outer boundary layer and far-field solutions in place, the necessary constants may be determined via matching appropriate limiting forms of the solutions to each other. The details of the intermediate steps of the calculation and the exact

expressions are given in the supplementary material. The growth rate from the matching exercise arises at $O(gE^2)$, with $g = \exp(-(1/(m-1))(\sqrt{2/E}))$, and is given by the following expression:

$$c_{3i} = -4\sqrt{2}\pi \mathrm{e}^{6/(m-1)} \left(32\sqrt{2} + \frac{4}{3}(m^2-1)(2m-1) + \frac{8\sqrt{2}}{3}(m^2-1) \right). \tag{3.43}$$

The negative sign in (3.43) corresponds to an unstable mode. Figure 8(*a*) shows a comparison between the asymptotic expression in (3.43) and the numerical results in an appropriate scaled form. Although, as shown in figure 8(*a*), the numerical results do not extend until an E small enough for a near-quantitative agreement with the analytical prediction, the numerical curve nevertheless turns around at $E \approx 0.02$, with there being a clear indication of an eventual convergence to the analytical asymptote.

As already mentioned, the emergence of the transcendentally small length scale (and the similarly small scaling for the growth rate) implies that the numerics breaks down at a slightly smaller E ($\approx$0.016) for the resolution used in figure 8(*a*) ($\tilde{N} = 8000$). Continuing the numerical curve down to smaller E would require an exponential increase in resolution; some evidence of the modest increase in the range of validity of the numerics, even with substantial increase in resolution, is provided in figure 8(*b*).

4. Conclusions

In this paper, we have described a novel inertio–elastic instability of a vortex column in a dilute polymer solution. The regime analysed pertains to large Reynolds (Re) and Deborah (De) numbers, involving a balance of inertia and elasticity at leading order, and the instability is governed by the elastic equivalent of the Rayleigh equation for swirling flows; momentum diffusion and relaxation of the disturbance polymeric stresses being neglected. The instability arises due to the resonant interaction of elastic shear waves made possible by the background shear in the irrotational exterior of the vortex column. The dimensionless parameter that appears in the elastic Rayleigh equation, and that governs the growth rate of the unstable mode, is the elasticity number $E = De(1-\beta)/Re$.

The existence of the inertio–elastic instability is first demonstrated numerically for the Rankine vortex, for finite E, as a function of the azimuthal wavenumber m. A matched asymptotic expansions approach, valid for small E, helps extend the numerical results down to $E = 0$, and thereby shows the absence of an elasticity threshold for instability. That is to say, the Rankine vortex is unstable for any finite E in the limit $De, Re \to \infty$, although the (dimensional) growth rate is transcendentally small, scaling as $O(\Omega_0 E^2 \mathrm{e}^{-1/E^{1/2}})$ for $E \to 0$. Importantly, the finite-E growth rate is not small, with a maximum of $O(0.1\Omega_0)$ (figure 4*d*). The numerical investigation further shows that the instability persists for smooth monotonically decreasing vorticity profiles – at least the 'intense' Rankine-like profiles which exhibit a rapid variation from the central rigidly rotating core to the irrotational exterior. This finding is in contrast to previous work in this regard for parallel shear flows. For instance, although the growth rate associated with the analogous inertio–elastic instability for submerged jets also appears to be transcendentally small for small E (see figure 7 of Rallison & Hinch (1995)), the authors believed the instability to be essentially dependent on the discontinuity in the first normal stress difference profile that arises from the assumed abrupt transition of the base state jet profile to a quiescent ambient at either end (where the jet velocity equals zero – see Miller (2005)). Thus, the instability was speculated to be absent for smoothed versions of such

jet profiles. However, the present results suggest that a slightly smoothed version of the original parabolic jet will also be subject to an analogous inertio–elastic instability. We have verified the same by analysing a smoothed version of the parabolic jet profile using a spectral calculation (not shown); an analytical approach is not possible in this case, owing to the insolubility of the inviscid ($E = 0$) Rayleigh equation for the plane Poiseuille profile.

An estimate of the region in the *De*–*Re* plane where one expects the shear-wave instability above to be largely unmodified may be obtained by requiring that the thickness of the viscous critical layer (assumed to be of $O(Re^{-1/3})$ similar to the classical Newtonian case; see Drazin & Reid (1981)) be much smaller than the $O(\sqrt{E})$ inviscid elastic boundary layer. This translates to the requirement $De \gg Re^{1/3} \gg 1$; this requirement is also consistent with the relaxation boundary layer of $O(De^{-1})$ being asymptotically thinner than the elastic one. The elastic Rayleigh limit (De/Re fixed, De, $Re \gg 1$) is entirely consistent with this estimate. Note, however, that a large but finite *Re* or *De* will lead to the emergence of a weak elasticity threshold for the onset of the instability.

There is an exact analogy between the viscoelastic flows studied here, in the limit $De \to \infty$, and MHD flows in the limit of infinite magnetic Reynolds number (Re_m) (Ogilvie & Proctor 2003; Ogilvie & Potter 2008; Vieu & Mutabazi 2019); here $Re_m = \mu_s/(\rho\lambda_m)Re$ for a conducting fluid of density ρ, viscosity μ_s and magnetic diffusivity λ_m. Thus, the elastic shear waves examined here are the analogue of Alfvén waves in the MHD context. An analogue of the instability discussed in this paper thus likely exists in the astrophysical setting of accretion discs. In particular, accretion discs with a rapid transition in the azimuthal magnetic field would be susceptible to a Alfvén-wave resonance instability, similar to the shear-wave resonance instability described herein (Balbus & Hawley 1991). Further, the matched asymptotic expansions approach involving multiple boundary layers, presented here, may be extended to gain insight into the classical non-axisymmetric magnetorotational instability (Ogilvie & Pringle 1996; Khalzov *et al.* 2006) as well as MHD instabilities in parallel shear flows (Stern 1963; Heifetz *et al.* 2015). Although a detailed comparison must await an analysis of three-dimensional perturbations, there are features associated with earlier numerical spectral calculations in the former case that bear the hallmark of a transcendentally small length scale (Ogilvie & Pringle 1996).

In the Newtonian limit, the Rankine vortex is centrifugally stable (according to the Rayleigh criterion), and this, together with the absence of a vorticity maximum at a finite radius, implies stability to both two- and three-dimensional disturbances (Drazin & Reid 1981). As pointed out above, the two-dimensional inertio–elastic instability of the Rankine vortex analysed here is expected to have an MHD analogue. Further, monotonically decreasing quasi-Keplerian angular velocity profiles characterizing accretion disks are known to be susceptible to the magnetorotational instability (Ogilvie & Pringle 1996). The MHD analogy thus implies that the Rankine vortex, and smooth Rankine-like profiles, will be susceptible to an additional inertio–elastic instability when three-dimensional perturbations, with a finite axial wavenumber, are taken into account. One expects novel features to emerge, both with regard to the CS and in terms of a denumerable infinity of discrete modes. Earlier efforts in this regard, both computations (Ogilvie & Potter 2008) and experiments (Groisman & Steinberg 1996; Boldyrev, Huynh & Pariev 2009; Dutcher & Muller 2011, 2013; Bai, Crumeyrolle & Mutabazi 2015) have only explored the domain of existence for moderate *Re* and *De*, and for the Taylor–Couette geometry. Extending these efforts to the case of large but finite *Re* and *De* would help precisely delineate the domain of existence of the inertio–elastic instability.

The present inertio–elastic instability also shares similarities with the widely studied stratorotational instability, which is also postulated as a mechanism for (outward) angular

momentum transport in cold weakly ionized accretion disks (Dubrulle *et al.* 2005). The latter arises from a resonance between Kelvin waves and/or inertia-gravity waves and also exhibits a transcendentally small scaling for small Rossby number (Yavneh, McWilliams & Molemaker 2001; Vanneste & Yavneh 2007). Nevertheless, there are important differences between the two cases. Most importantly, the stratorotational instability only occurs for three-dimensional perturbations. Further, the locations of the Kelvin waves are fixed in the neighbourhood of the two walls and hence the spacing between the resonating modes is fixed by the gap width; this, along with the exponential trapping of the individual waves, explains the transcendental scaling above. On the other hand, for the inertio–elastic instability, the spacing is fixed by the region where inertial and elastic stresses are of comparable magnitude (the elastic boundary layer). Finally, the eigenmode of the usual stratorotational instability does not become singular in the limit of zero growth rate (Yavneh *et al.* 2001; Vanneste & Yavneh 2007). The present scenario thus more closely resembles the recently studied case where the stratorotational instability results from a resonant interaction between a Kelvin/inertia-gravity wave with a baroclinic critical level (Wang & Balmforth 2018).

Finally, the inertio–elastic instability examined here may be important to the general dynamics of polymeric flows at large Re. Simplistically speaking, the vortex column analysed in this paper may be likened to an eddy in the turbulent cascade scenario where the time scale is short enough for elastic stresses to become comparable to inertial stresses, while at the same time being much more important than viscosity. The interaction between vortices and polymers has been shown to play a crucial role in the buffer layer structure of wall-bounded turbulent flows of dilute polymer solutions (Roy *et al.* 2006; Kim *et al.* 2007; White & Mungal 2008; Tabor & de Gennes 1986). The instability studied in this paper can be a starting point to form a deeper mechanistic understanding of the same.

Supplementary material. Supplementary material is available at https://doi.org/10.1017/jfm.2022.122.

Acknowledgments. This work has benefitted from discussions with Professor G.M. Homsy. A.R. would also like to acknowledge IIT Madras for its support of the 'Geophysical Flows Lab' research initiative under the Institute of Eminence framework.

Declaration of interests. The authors report no conflict of interest.

Author ORCIDs.
Anubhab Roy https://orcid.org/0000-0002-0049-2653;
Piyush Garg https://orcid.org/0000-0001-7935-5805;
Jumpal Shashikiran Reddy https://orcid.org/0000-0001-8788-7588;
Ganesh Subramanian https://orcid.org/0000-0003-4314-3602.

References

Avgousti, M. & Beris, A.N. 1993 Viscoelastic Taylor–Couette flow: bifurcation analysis in the presence of symmetries. *Proc. R. Soc. Lond.* A **443**, 17–37.

Azaiez, J. & Homsy, G.M. 1994*a* Linear stability of free shear flow of viscoelastic liquids. *J. Fluid Mech.* **268**, 37–69.

Azaiez, J. & Homsy, G.M. 1994*b* Numerical simulation of non-newtonian free shear flows at high Reynolds numbers. *J. Non-Newtonian Fluid Mech.* **52**, 333–374.

Bai, Y., Crumeyrolle, O. & Mutabazi, I. 2015 Viscoelastic Taylor–Couette instability as analog of the magnetorotational instability. *Phys. Rev.* E **92** (3), 031001.

Balbus, S.A. & Hawley, J.F. 1991 A powerful local shear instability in weakly magnetized disks. I. Linear analysis. *Astrophys. J.* **376**, 214–222.

Beard, D.W., Davies, M.H. & Walters, K. 1966 The stability of elastico-viscous flow between rotating cylinders. Part 3. Overstability in viscous and Maxwell fluids. *J. Fluid Mech.* **24**, 321–334.

BIRD, R.B., ARMSTRONG, R.C. & HASSAGER, O. 1987 *Dynamics of polymeric liquids. Volume 1 – Fluid Mechanics*. John Wiley and Sons.

BOLDYREV, S., HUYNH, D. & PARIEV, V. 2009 Analog of astrophysical magnetorotational instability in a Couette–Taylor flow of polymer fluids. *Phys. Rev.* E **80** (6), 066310.

BOYD, J.P. 1999 The devil's invention: asymptotic, superasymptotic and hyperasymptotic series. *Acta Appl. Math.* **56**, 1–98.

BRIDGES, T.J. & MORRIS, P.J. 1984 Differential eigenvalue problems in which the parameter appears nonlinearly. *J. Comput. Phys.* **55**, 437–460.

CASE, K.M. 1960 Stability of inviscid plane Couette flow. *Phys. Fluids* **3**, 143.

CHANDRA, B., SHANKAR, V. & DAS, D. 2018 Onset of transition in the flow of polymer solutions through microtubes. *J. Fluid Mech.* **844**, 1052–1083.

CHAUDHARY, I., GARG, P., SHANKAR, V. & SUBRAMANIAN, G. 2019 Elasto-inertial wall mode instabilities in viscoelastic plane poiseuille flow. *J. Fluid Mech.* **881**, 119–163.

CHAUDHARY, I., GARG, P., SUBRAMANIAN, G. & SHANKAR, V. 2021 Linear instability of viscoelastic pipe flow. *J. Fluid Mech.* **908**, A11.

CHOUEIRI, G.H., LOPEZ, J.M. & HOF, B. 2018 Exceeding the asymptotic limit of polymer drag reduction. *Phys. Rev. Lett.* **120** (12), 124501.

DABADE, V., NAVANEETH, K.M. & SUBRAMANIAN, G. 2015 Effects of inertia and viscoelasticity on sedimenting anisotropic particles. *J. Fluid Mech.* **778**, 133–188.

DRAZIN, P.G. & HOWARD, L.N. 1966 Hydrodynamic stability of parallel flow of inviscid fluid. *Adv. Appl. Mech.* **9**, 1–89.

DRAZIN, P.G. & REID, W.H. 1981 *Hydrodynamic Stability*. Cambridge University Press.

DUBIEF, Y., WHITE, C.M., TERRAPON, V.E., SHAQFEH, E.S.G., MOIN, P. & LELE, S.K. 2004 On the coherent drag-reducing and turbulence-enhancing behavior of polymers in wall flows. *J. Fluid Mech.* **514**, 271–280.

DUBRULLE, B, MARIE, L., NORMAND, C., RICHARD, D., HERSANT, F. & ZAHN, J.-P. 2005 A hydrodynamic shear instability in stratified disks. *Astron. Astrophys.* **429** (1), 1–13.

DUTCHER, C.S. & MULLER, S.J. 2011 Effects of weak elasticity on the stability of high Reynolds number co- and counter-rotating Taylor–Couette flows. *J. Rheol.* **55** (6), 1271–1295.

DUTCHER, C.S. & MULLER, S.J. 2013 Effects of moderate elasticity on the stability of co- and counter-rotating Taylor–Couette flows. *J. Rheol.* **57** (3), 791–812.

ENGEVIK, L. 1971 A note on a stability problem in hydrodynamics. *Acta Mech.* **12**, 143–153.

GAKHOV, F.D. 1990 *Boundary Value Prolems*. Dover.

GARG, P., CHAUDHARY, I., KHALID, M., SHANKAR, V. & SUBRAMANIAN, G. 2018 Viscoelastic pipe flow is linearly unstable. *Phys. Rev. Lett.* **121** (2), 024502.

GORODTSOV, V. & LEONOV, A. 1967 On a linear instability of a plane parallel Couette flow of viscoelastic fluids. *J. Appl. Math. Mech.* **31**, 289–299.

GRAHAM, M.D. 1998 Effect of axial flow on viscoelastic Taylor–Couette instability. *J. Fluid Mech.* **360**, 341–374.

GRAHAM, M.D. 2014 Drag reduction and the dynamics of turbulence in simple and complex fluids. *Phys. Fluids* **26** (10), 101301.

GROISMAN, A. & STEINBERG, V. 1996 Couette–Taylor flow in a dilute polymer solution. *Phys. Rev. Lett.* **77** (8), 1480.

GROISMAN, A. & STEINBERG, V. 2000 Elastic turbulence in a polymer solution flow. *Nature* **405**, 53–55.

HAJ-HARIRI, H. & HOMSY, G.M. 1997 Three-dimensional instability of viscoelastic elliptic vortices. *J. Fluid Mech.* **353**, 357–381.

HEIFETZ, E., MAK, J., NYCANDER, J. & UMURHAN, O.M. 2015 Interacting vorticity waves as an instability mechanism for magnetohydrodynamic shear instabilities. *J. Fluid Mech.* **767**, 199–225.

HOWARD, L.N. 1962 Note on a paper of John W. Miles. *J. Fluid Mech.* **10**, 509–512.

JAMES, D.F. 2009 Boger fluids. *Ann. Rev. Fluid Mech.* **41**, 129–142.

JOSEPH, D.D. 2007 *Fluid Dynamics of Viscoelastic Liquids*. Springer.

KERSWELL, R.R. 2002 Elliptical instability. *Annu. Rev. Fluid Mech.* **34**, 83.

KHALZOV, I.V., ILGISONIS, V.I., SMOLYAKOV, A.I. & VELIKHOV, E.P. 2006 Magnetorotational instability in electrically driven flow of liquid metal: spectral analysis of global modes. *Phys. Fluids* **18** (12), 124107.

KIM, K., LI, C.-F., SURESHKUMAR, R., BALACHANDAR, S. & ADRIAN, R.J. 2007 Effects of polymer stresses on eddy structures in drag-reduced turbulent channel flow. *J. Fluid Mech.* **584**, 281–299.

KUPFERMAN, R. 2005 On the linear stability of plane Couette flow for an Oldroyd-B fluid and its numerical approximation. *J. Non-Newtonian Fluid Mech.* **127**, 169–190.

LARSON, R.G. 1988 *Constitutive Equations for Polymer Melts and Solutions*. Butterworths.

LARSON, R.G. 1992 Instabilities in viscoelastic flows. *Rheol. Acta* **31**, 213–263.
LARSON, R.G., SHAQFEH, E.S.G. & MULLER, S.J. 1990 A purely elastic instability in Taylor–Couette flow. *J. Fluid Mech.* **218**, 573–600.
LUMLEY, J.L. 1969 Drag reduction by additives. *Annu. Rev. Fluid Mech.* **1**, 367–384.
MILLER, J.C. 2005 *Shear flow instabilities in viscoelastic fluids*. PhD thesis, Cambridge University Press.
MOORE, D.W. & SAFFMAN, P.G. 1975 The instability of a straight vortex filament in a strain field. *Proc. R. Soc. Lond.* A **346**, 413–425.
OGILVIE, G.I. & POTTER, A.T. 2008 Magnetorotational-type instability in Couette–Taylor flow of a viscoelastic polymer liquid. *Phys. Rev. Lett.* **100**, 074503.
OGILVIE, G.I. & PRINGLE, J.E. 1996 The non-axisymmetric instability of a cylindrical shear flow containing an azimuthal magnetic field. *Mon. Not. R. Astron. Soc.* **279** (1), 152–164.
OGILVIE, G.I. & PROCTOR, M.R.E. 2003 On the relation between viscoelastic and magnetohydrodynamic flows and their instabilities. *J. Fluid Mech.* **476**, 389–409.
RALLISON, J.M. & HINCH, E.J. 1995 Instability of a high-speed submerged elastic jet. *J. Fluid Mech.* **288**, 311–324.
RENARDY, M. 2008 Stability of viscoelastic shear flows in the limit of high Weissenberg and Reynolds numbers. *J. Non-Newtonian Fluid Mech.* **155**, 124–129.
RENARDY, M. & RENARDY, Y. 1986 Linear stability of plane Couette flow of an upper convected Maxwell fluid. *J. Non-Newtonian Fluid Mech.* **22**, 23–33.
ROY, A. 2013 Singular eigenfunctions in hydrodynamic stability: The roles of rotation, stratification and elasticity. PhD thesis, JNCASR.
ROY, A., MOROZOV, A., VAN SAARLOOS, W. & LARSON, R.G. 2006 Mechanism of polymer drag reduction using a low-dimensional model. *Phys. Rev. Lett.* **97** (23), 234501.
ROY, A. & SUBRAMANIAN, G. 2014*a* An inviscid modal interpretation of the 'lift-up' effect. *J. Fluid Mech.* **757**, 82–113.
ROY, A. & SUBRAMANIAN, G. 2014*b* Linearized oscillations of a vortex column: the singular eigenfunctions. *J. Fluid Mech.* **741**, 404–460.
SAMANTA, D., DUBIEF, Y., HOLZNER, M., SCHAFER, C., MOROZOV, A.N., WAGNER, C. & HOF, B. 2013 Elasto-inertial turbulence. *Proc. Natl Acad. Sci.* **110**, 10557–10562.
SHAQFEH, E.S.G. 1996 Purely elastic instabilities in viscometric flows. *Annu. Rev. Fluid Mech.* **28**, 129–185.
SHEKAR, A., MCMULLEN, R.M., WANG, S.-N., MCKEON, B.J. & GRAHAM, M.D. 2019 Critical-layer structures and mechanisms in elastoinertial turbulence. *Phys. Rev. Lett.* **122** (12), 124503.
STERN, M.E. 1963 Joint instability of hydromagnetic fields which are separately stable. *Phys. Fluids* **6** (5), 636–642.
SURESHKUMAR, R., BERIS, A.N. & HANDLER, R.A. 1997 Direct numerical simulation of turbulent channel flow of a polymer solution. *Phys. Fluids* **9**, 743–755.
TABOR, M. & DE GENNES, P.G. 1986 A cascade theory of drag reduction. *Europhys. Lett.* **2**, 519–522.
THOMAS, R.H. & WALTERS, K. 1964 The stability of elastico-viscous flow between rotating cylinders. Part 1. *J. Fluid Mech.* **18**, 33–43.
THOMAS, R.H. & WALTERS, K. 1965 On the flow of an elastico-viscous liquid in a curved pipe of elliptic cross-section under a pressure-gradient. *J. Fluid Mech.* **21**, 173–182.
THOMAS, R.H. & WALTERS, K. 1966 The stability of elastico-viscous flow between rotating cylinders. Part 2. *J. Fluid Mech.* **19**, 557–560.
VANNESTE, J. & YAVNEH, I. 2007 Unbalanced instabilities of rapidly rotating stratified shear flows. *J. Fluid Mech.* **584**, 373–396.
VIEU, T. & MUTABAZI, I. 2019 A theory of magnetic-like fields for viscoelastic fluids. *J. Fluid Mech.* **865**, 460–491.
VIRK, P.S. 1975 Drag reduction fundamentals. *AIChE J.* **21**, 625–656.
WANG, C. & BALMFORTH, N.J. 2018 Strato-rotational instability without resonance. *J. Fluid Mech.* **846**, 815–833.
WHITE, C.M. & MUNGAL, M.G. 2008 Mechanics and prediction of turbulent drag reduction with polymer additives. *Annu. Rev. Fluid Mech.* **40**, 235–256.
WILSON, H., RENARDY, M. & RENARDY, Y. 1999 Structure of the spectrum in zero Reynolds number shear flow of the UCM and Oldroyd-B liquids. *J. Non-Newtonian Fluid Mech.* **80**, 251–268.
YARIN, A.L. 1997 On the mechanism of turbulent drag reduction in dilute polymer solutions: dynamics of vortex filaments. *J. Non-Newtonian Fluid Mech.* **69**, 137–153.
YAVNEH, I., MCWILLIAMS, J.C. & MOLEMAKER, M.J. 2001 Non-axisymmetric instability of centrifugally stable stratified Taylor–Couette flow. *J. Fluid Mech.* **448**, 1–21.